The Journal of Chemical Physics

RESEARCH ARTICLE | JUNE 30 2025

Water ice formed by vapor deposition and liquid aerosol injection: A comparison study using reflectance absorption infrared spectroscopy

Christina E. Buffo ; Brant M. Jones ; Thomas M. Orlando

J. Chem. Phys. 162, 244509 (2025)
https://doi.org/10.1063/5.0261149

The Journal of Chemical Physics ARTICLE pubs.aip.org/aip/jcp

Water ice formed by vapor deposition and liquid aerosol injection: A comparison study using reflectance absorption infrared spectroscopy

Cite as: J. Chem. Phys. 162, 244509 (2025); doi: 10.1063/5.0261149
Submitted: 29 January 2025 • Accepted: 29 May 2025 •
Published Online: 30 June 2025

Christina E. Buffo,[1] Brant M. Jones,[1,2] and Thomas M. Orlando[1,2,3,a)]

AFFILIATIONS

[1] School of Chemistry and Biochemistry, Georgia Institute of Technology, Atlanta, Georgia 30332, USA
[2] Center for Space Technology and Research, Georgia Institute of Technology, Atlanta, Georgia 30332, USA
[3] School of Physics, Georgia Institute of Technology, Atlanta, Georgia 30332, USA

[a)] **Author to whom correspondence should be addressed:** thomas.orlando@chemistry.gatech.edu

ABSTRACT

Low temperature water ices (90–165 K) were produced via flash freezing during liquid aerosol injection (LAI) or vapor deposition (VD). The infrared spectral shapes of the O–H stretch at 3 μm (3300 cm^{-1}) and the H–O–H bend at 6 μm (1600 cm^{-1}) indicate that the two deposition methods produce different ice structures, with VD producing predominately more ordered structures than LAI at every deposition temperature studied. These different amorphous structures behave similarly with heating but remain spectrally different until crystallization, consistent with previous findings that hyperquenched glassy water and amorphous solid water are structurally different. This work demonstrates the utility of studies with experimental systems capable of directly comparing ice formation methods. To determine the presence of crystalline ice, the shape of the 3-μm feature is most useful, while the intensity of the 6-μm feature is a reliable indicator of amorphous ice and liquid-like behavior of the ice with heating. Liquid-like phases can be produced through LAI at all temperatures studied and through VD at the glass transition temperature of 136 K.

INTRODUCTION

Water has many unique properties that underpin its general importance on Earth and throughout the solar system. In particular, many crystalline and amorphous phases with variable structures, densities, and porosities can exist depending on the formation temperatures and pressures.[1,2] In addition to the well-ordered crystalline ice (CI) phases, amorphous ice can be classified as low-density amorphous (LDA), high-density amorphous (HDA), and very high-density amorphous (VHDA) ices. Recent studies suggest one or more forms of medium-density amorphous (MDA) ice may also exist[1,3,4] and that amorphous ices may be made of randomly oriented nanocrystalline hexagonal and cubic ice.[5] LDA can be formed by vapor deposition at low temperature (<150 K) and pressure (<1 × 10^{-4} Torr) conditions. Low density amorphous ice formed through vapor deposition has also been called amorphous solid water (ASW). Slow formation, through a "hit-and-stick" approach of individual gas molecules freezing in place on a cooled surface, allows control of morphology via backing pressure and deposition angle. Ice formed at higher deposition angles, especially those of more than 60° from normal, tends to have increased porosity and larger apparent surface areas than those formed with near normal angles.[6–8] The LDA, HDA, VHDA, and MDA forms can be distinguished experimentally from crystalline ices and from each other by their density, infrared spectra, and thermodynamic behavior. While the extremes of pressure and low temperatures cause these amorphous ices to exist primarily in laboratory settings on Earth, in the interstellar media, vapor-deposited LDA (ASW) may be the most common form of ice in the universe.[1,9,10]

The formation mechanism of amorphous ice can influence its properties, and these differences have led to the naming of specific sub-states. Hyperquenched glassy water (HGW) is one such sub-state with minimal intermediate range order (beyond nearest neighboring molecules): it is formed by rapidly cooling liquid water at constant pressure with a rate of more than 10^{7} K s^{-1}.[1,2,11,12] This supercooling prevents the formation of well-ordered crystalline ice,

even in temperature and pressure conditions that favor crystallization. Instead, a glass structure is produced, retaining many of the characteristics of liquid water, including a lack of pores.[11,13–16] Differences in the infrared spectra of this and other LDA substates are known.[17] However, oxygen–oxygen radial distances from neutron scattering data[18,19] and XRD data for low density amorphous forms appear very similar.[5,19–22] Infrared (IR) spectral differences are typically probed by examining the shape of the O–H stretch feature between 2.77 and 3.22 μm (3100–3600 cm^{-1}), since this stretch is known to be phase- and temperature-sensitive.[23] While hexagonal (I_h) and cubic (I_c) crystalline ices have nearly identical spectra in the near infrared,[4,24,25] non-crystalline ices can be spectrally distinguished from crystalline ice. Non-crystalline ice has a 3-μm band dominated by a higher-energy component at 2.9 μm (3400 cm^{-1}) corresponding to 2 or 3 coordinate molecules with dangling bonds, while crystalline ice has a 3-μm band dominated by a lower-energy feature at 3.1 μm (3250 cm^{-1}) associated with more ordered fully 4 coordinate states.[26,27]

The H–O–H bend at 6 μm (1660 cm^{-1}) is also phase- and temperature-sensitive.[21,27] Although the oscillator strength is much weaker than the 3-μm feature due to interactions with librational modes, it is particularly useful in remote observations of rocky, airless bodies such as the Moon[28,29] because it is specific to molecular water, while the 3-μm band is sensitive to both water and hydroxyl groups. The 6-μm feature is pronounced in liquid water and in flash-frozen droplets and water clusters. In the latter cases, the bending mode is correlated primarily to the presence of double-donor 3 coordinate surface molecules and is prominent for cluster sizes above 20 nm.[27]

Deposition of liquid aerosols and flash freezing of water using aerosol jets have been used primarily to probe supercooled water, where the freezing out of the disordered structure prior to crystallization allows the study of a possible thermodynamic connection of HGW and ASW to the liquid state. Extremely rapid cooling conditions (>10^7 K s^{-1}) are not as common in space as the slow vapor deposition processes that produce ASW in the interstellar medium and other low-pressure environments such as the permanently shadowed regions of the Moon.[6,30–35] However, flash freezing conditions may occur during cryovolcanic eruptions or refreezing of ice following a transient heating event such as a micrometeorite impact.[36,37] Though the two main methods of ice formation under low temperature and pressure, vapor deposition (VD) and liquid aerosol injection (LAI) followed by flash freezing, have been studied extensively, they have not been directly compared in the same experimental system. This paper reports a detailed comparison of the temperature- and phase-dependent infrared signatures of ices formed by vapor deposition and liquid aerosol injection to provide constraints on the structures that are formed under low temperature and pressure formation conditions.

EXPERIMENTAL APPROACH

Experiments were performed in a high vacuum (HV) chamber (base pressure of $<1 \times 10^{-8}$ Torr) coupled to a Fourier Transform Infrared (FTIR) spectrometer (Bruker Equinox 55) equipped with an external liquid nitrogen cooled HgCdTe detector (Fig. 1). Pressures were maintained by a turbomolecular pump (Pfeiffer Vacuum TC600) backed by a scroll pump (Edwards XDS 5), and pressures

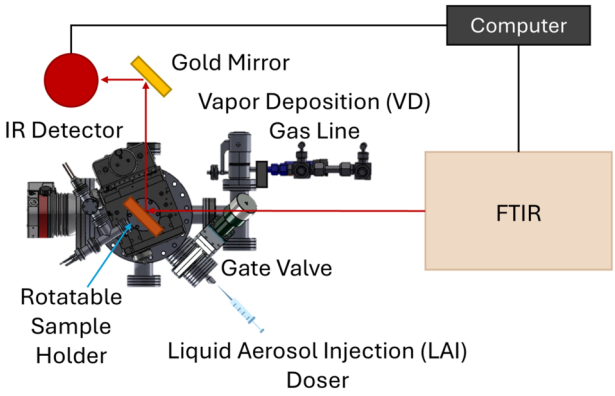

FIG. 1. Ices were formed by positioning the rotatable sample holder normal to either the gate valve and syringe (liquid aerosol injection) or the gas dosing line (vapor deposition). The IR beam path (red arrows) originates from the FTIR, then passes through an IR transparent window to hit the sample holder. After reflecting off the sample holder, the beam passes through another IR window before reaching the detector. Pumps and pressure gauges are not shown.

were monitored with a hot cathode ion gauge (not shown) and a vacuum gauge controller (Granville Phillips 307).

Within the HV system, ice was grown on a vertically mounted rotatable copper sample holder cooled by liquid nitrogen. The copper sample holder, which was chosen for its high thermal conductivity, could be rotated to be normal to the vacuum gas dosing line or normal to the liquid aerosol injection dosing port for controlled deposition/growth. To collect IR spectra, the sample holder was positioned at a 45° angle relative to incoming light from the FTIR, and reflected light was collected at a 90° angle relative to the incoming light. Differentially pumped IR-transparent KBr windows were used.

The sample holder temperature was monitored by a K-type thermocouple attached to the copper sample holder. The coldest temperature attainable was ~90 K. The other formation temperatures (113, 135, 140, and 165 K, all ±2 K) were set by a 25 Ω 100 W resistive heating cartridge and chosen to represent ices formed above and below the glass transition at 136 K.[11,12,15,30,38,39] All ices were created with high-performance liquid chromatography-mass spectrometry (HPLC-MS) grade water. The water used for vapor deposition was freeze-pump-thawed with liquid nitrogen three times to remove residual atmospheric gases. After ice formation (see following sections), the ices were cooled to ~90 K. The sample holder was then heated at a steady rate of 1 K min^{-1} by a LakeShore 336 Temperature Controller. Reflectance Infrared Absorption Spectroscopy (RAIRS) measurements were collected every 1 min (1 K) during heating until sublimation at ~185 K, and the ices are assumed to be in thermal equilibrium during spectra collection. Each spectrum is an average of 64 scans and has a spectral resolution of 1.9 cm^{-1}. The measurements used a zero-filling factor of 2, a Blackman-Harris 3-Term apodization function, and a Mertz phase correction mode.

Liquid aerosol injection

The LAI system consisted of a simple 20-gauge needle syringe filled with 20 μl of water under room temperature and atmospheric pressure conditions. This water was then injected through a

septum into the HV chamber to produce a jet of micrometer-sized aerosol droplets.[40–42] The droplets then cool through adiabatic expansion and evaporation during their movement through the vacuum, resulting in cooling and mass loss. The large surface area and cold temperature of the sample holder cause rapid temperature changes and vitrification in the incident water immediately on contact.[15] This process, also called splat cooling, occurs due to the decrease in pressure from atmosphere to vacuum and due to the copper sample holder temperature extraction rate, which is estimated to be ~10^7 K s^{-1}. Assuming an ice density of ~0.9 g/cm[43] and that 60%–90% of the volume of the injected liquid froze on the surface, ice thicknesses were ~5500–8500 ML (monolayers) or about 2–3 μm. During LAI, the maximum pressure within the HV system was ~0.1 Torr for the <1 s required to inject the entire solution, after which the pressure immediately dropped to less than 1×10^{-3} Torr. When not used for LAI, the septum was separated from the HV chamber by a gate valve (Fig. 1). This permitted shorter exposures to increased pressures during injection and allowed chamber pressures of $<1 \times 10^{-8}$ Torr with the gate valve closed.

In these thick ices, incident infrared light is primarily absorbed by bulk water with minimal contributions from the water–copper interface and the water–vacuum interface. The prominence of crystalline vs amorphous IR features, therefore, primarily represents the bulk composition rather than the surface structure. Thick ices also minimize the influence of atmospheric water vapor that leaks into the chamber during LAI.[12]

Comparisons can be made between the thicker ice in this study and thinner (hundreds of ML) bulk ice. Thicker ices will have higher peak desorption temperatures than thin ices[44,45] and higher crystallization temperatures.[46–48] However, while the spectral intensity in thicker ices will be more than in thinner ices, the features themselves will not change, and phases can be assigned comparably to thinner ices. Ices up to 3 μm thick have been treated as comparable to 100 nm and 100 ML ices for Raman and IR absorbance, especially in the astrochemistry literature.[49–51]

Vapor deposition

Vapor deposition was performed by dosing water through a precision leak valve with a backing pressure of 1×10^{-5} Torr, which translates to a dose rate of 10 ML s^{-1}.[52] The vacuum chamber and gas line geometries (Fig. 1) prevented water molecules from hitting the sample holder directly to avoid a preferred orientation for ice growth. Water was dosed until the band depth measured at 3 μm (3300 cm^{-1}) approached that of ices formed through liquid aerosol injection. Under these conditions, ice thickness was measured at ~7500 ML, or about 2 μm, based on HeNe laser constructive and destructive interference patterns (Fig. S1).[53–55]

HeNe laser estimates were not used for LAI because changes in the interference patterns are sinusoidal. This sinusoidal evolution is only visible for slow formation, and a difference in the absolute value of an absorbance measurement before and after injection could be consistent with a number of different ice thicknesses. This method was used to verify ice thickness estimates from IR band depth, which may be misleading for RAIRS measurements.[56] All spectra were normalized to overcome that limitation and correct for potential small differences in sample holder angle during ice formation and RAIRS measurement collection.

RESULTS

Phases as a function of formation method

Spectra of the 3-μm (3300 cm^{-1}) O–H stretch (left) and 6-μm (1600 cm^{-1}) H–O–H bend (right) for ices formed by liquid aerosol injection (black solid line) and vapor deposition (gray dashed line) are shown in Fig. 2. At 165 K, vapor deposition (VD@165) produces pure crystalline ice (CI), with a 3-μm O–H stretch band dominated by a prominent feature at 3.1 μm (3200 cm^{-1}) [Fig. 2(a)]. This corresponds to tetrahedrally coordinated water molecules. Thermodynamically, water ice at 165 K in HV conditions should be crystalline. However, ices formed through liquid aerosol injection (LAI@165)

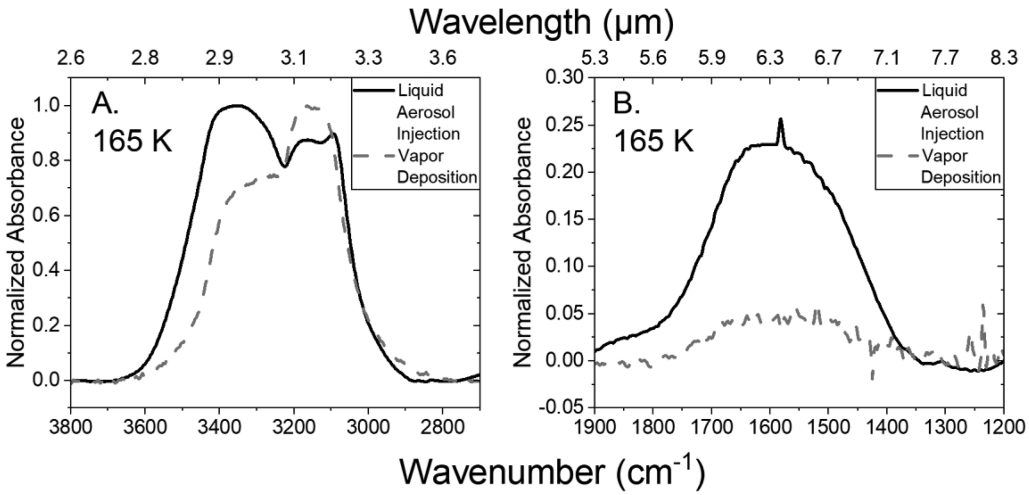

FIG. 2. Differences in the 3-μm (3300 cm^{-1}) O–H stretch (a) and 6-μm (1600 cm^{-1}) H–O–H bend (b) for ices formed by liquid aerosol injection (black solid line) and vapor deposition (gray dashed line) at 165 K. The vapor deposition spectrum matches published crystalline ice spectra, while the liquid aerosol injection does not. The plots preserve the relative intensity of the features by normalizing both to the maximum absorbance of the O–H stretch.

show a spectrum dominated by the longer wavenumber (higher energy) component of the O–H stretch at 2.9 μm (3400 cm^{-1}), consistent with less tetrahedral coordination and, therefore, more disorder. Figure 2(b) shows that VD@165 has a very weak 6-μm signal, as expected for CI due to its more constrained molecular geometry and smaller fraction of water molecules capable of bending. Neither the 3 nor 6 μm infrared feature is sufficient for distinguishing between hexagonal and cubic ice, so this crystalline ice could be either or a combination of both.[24] In contrast to VD, LAI@165 (i.e., rapid flash-freezing) leads to the formation of a disordered phase exhibiting a more intense 6-μm (1600 cm^{-1}) feature relative to the size of the 3-μm (3300 cm^{-1}) feature typical of undercoordinated (<4 coordinate) molecules.

For a more comprehensive picture of the dependence of phase on formation temperature, ices were formed at temperatures between 91 and 165 K through liquid aerosol injection and vapor deposition (Figs. 3 and 4). Specifically, Fig. 3 shows the three main phases of ice formed: CI produced by VD at 165 K (VD@165), HGW produced by LAI at 113 K (LAI@113), and ASW produced by LAI at 91 K (LAI@91). These phases were assigned based on comparisons to published spectra, including those that note the similarities of ASW to the overarching category of LDA.[17,57–61]

These well-characterized ice phase spectra are useful in unraveling the phase evolution as a function of deposition temperature.

Phases as a function of formation temperature

As shown in Fig. 4, at every formation temperature, LAI ices have a more prominent higher energy component of the O–H stretch at 2.9 μm (3400 cm^{-1}). For VD ices, a more prominent lower energy component at 3.1 μm (3200 cm^{-1}) is observed. The entire O–H stretch feature is also broader at every temperature for LAI vs VD ices. The VD ice trends are consistent with previous studies,[7,17,27,35,38,62–67] though the shape of the O–H stretch region in this study is broader than the IR features for ices formed by molecular beams due to molecular beams' precise control of the deposition angle and area.[6,8,17] In addition, the H–O–H bend feature at 6 μm (1600 cm^{-1}) is a factor of 2–3 larger for all ices formed by LAI compared to those formed at the same temperature through VD. The low-energy tail of the O–H bend seen at 7.1 μm (1400 cm^{-1}) for LAI can be attributed to IR-active hydrated protons formed during electrokinetic charging during LAI through a metal orifice.[68,69] No such charging occurs during VD.

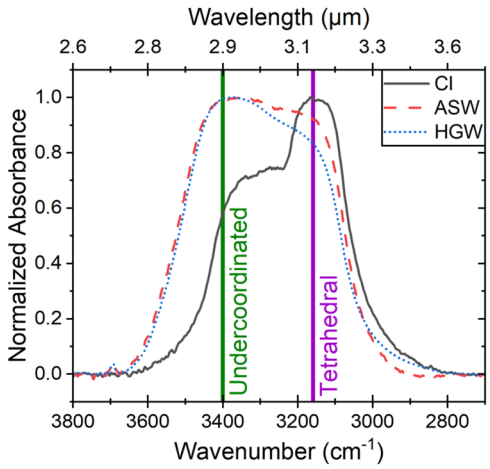

FIG. 3. Collected spectra corresponding to known phases of ice (see text). Normalized absorbance of the IR O–H stretch corresponding to crystalline ice (CI) (solid gray), amorphous solid water (ASW) ice (dashed red), and hyperquenched glassy water (HGW) (dotted blue). The CI spectrum is from vapor deposition at 165 K, ASW from liquid aerosol injection at 91 K, and HGW from liquid aerosol injection at 113 K. Each spectrum is normalized at its maximum absorbance. The approximate energies corresponding to undercoordinated (3400 cm^{-1}) and tetrahedrally coordinated (3250 cm^{-1}) molecules are labeled (see text).

DISCUSSION

Phase evolution with temperature and heating

Differences in the O–H and H–O–H band depths and positions with deposition temperature (Fig. 4) could be attributed to uncertainties in the amount of ice grown and, therefore, in ice thickness. However, care was taken to minimize these differences, and the consistent nature of a larger band depth at 6 μm (1600 cm^{-1}) relative to the 3-μm (3300 cm^{-1}) band for LAI compared to VD suggests that the differences can mainly be attributed to the degree of disorder in the ices. All spectra were normalized at the maximum absorbance of the 3-μm (3300 cm^{-1}) band to further emphasize spectral differences in band shape. Non-normalized spectra can be found in Fig. S2.

The redshift and increasing broadness of the O–H stretch with increasing temperature have been documented for ice clusters[27,62,66] and have been correlated with the presence of dangling bond states and double-donor three-coordinated surface molecules. Since spectra in this study were collected over the entire thickness of the water ice, they reflect both surface and subsurface structures. The arrangement of water molecules changes with temperature, and the degree of disorder is inversely correlated with formation temperature. For example, at 91 K, injection ices resemble published spectra for LDA with a more prominent higher-energy 2.9 μm (3400 cm^{-1}) component of the O–H stretch.[17] This reflects the comparatively large amount of two- and three-coordinated water molecules, which can be found on both the surface of the ice and on pore boundaries within the ice.[27] The size of the H–O–H bend is also more similar between the two formation methods at 91 K than at any other temperature, and 91 K is the only temperature where both formation methods produce spectra with a 2.7 μm (3700 cm^{-1}) dangling bond feature (see Fig. S3).

At 113 K, the two ices (LAI@113 and VD@113) have 3-μm (3300 cm^{-1}) bands that appear to be mirror images of each other. Most importantly, LAI@113 matches the O–H stretch for HGW,[17] whose formation typically requires cooling rates of more than 10^7 K s^{-1}.[1,2,11,12] Injected water undergoes adiabatic cooling toward the supercooled state and more rapid cooling upon impact, which leads to the formation of HGW. The cooling rate is estimated as $\geq 10^7$ K s^{-1}. LAI with smaller cooling rates would produce ASW-like structures instead of HGW.[61]

At ~136 K and at pressures <1 × 10^{-8} Torr, water undergoes a glass transition.[11,12,15,30,38,39] Ices formed through both methods near this temperature (LAI@135 and VD@135) show a splitting

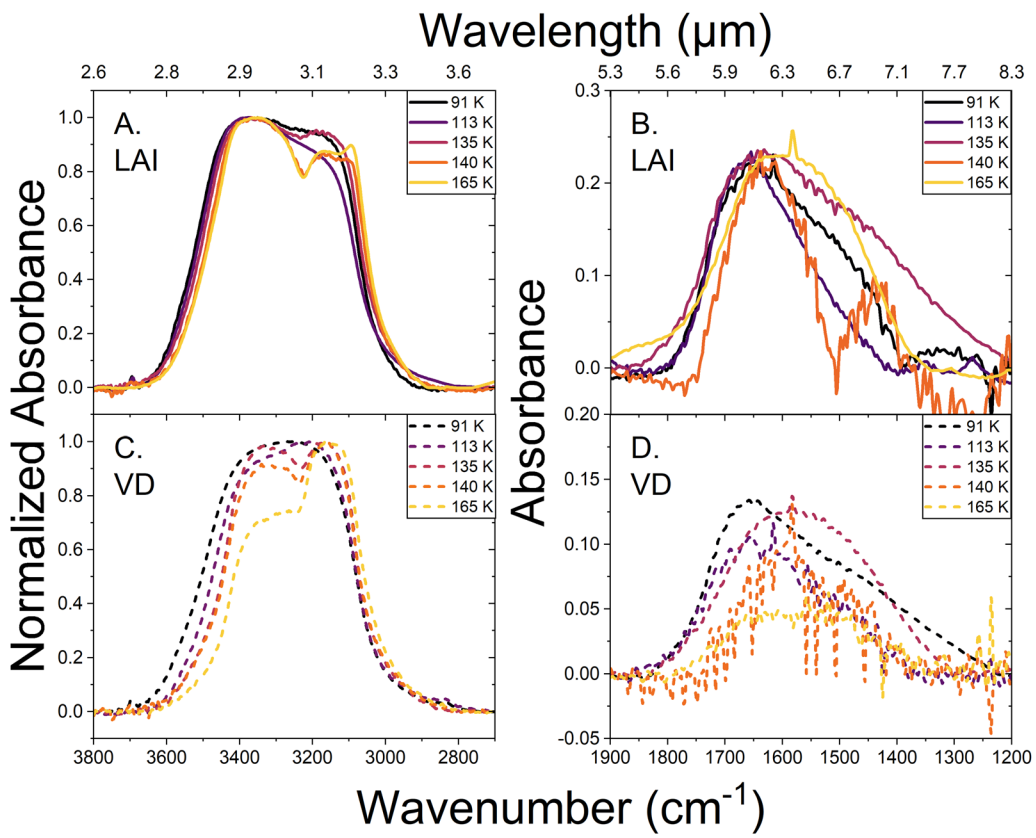

FIG. 4. Sections of the infrared spectra of ices formed by liquid aerosol injection (a) and (b) and vapor deposition (c) and (d), normalized to the maximum absorbance of the O–H stretch at 3 μm (3300 cm^{-1}) (left column). Ices were formed at the labeled temperature (91, 113, 135, 140, and 165 K), then cooled to ~91 K, where the shown spectra were taken. The left column shows the normalized O–H stretch after formation and before heating. The right column is the molecular water H–O–H bend at 6 μm (1600 cm^{-1}) for these same ices. The plots preserve the relative intensity of the features by normalizing both features to the O–H stretch.

between the high and low energy components of the O–H stretch, but VD@135 ice continues to have a larger contribution at lower vibrational energies due to a greater degree of tetrahedral coordination. The 6-μm (1600 cm^{-1}) band peak position is at slightly lower energies and has a smaller intensity for VD than for LAI, confirming that vapor deposition produces more crystalline ice.[62] At 140 K, both methods produce spectra comparable to formation at 165 K, but without such a strong difference in the relative O–H stretch component intensities due to fewer tetrahedrally coordinated molecules.

Heating experiments were conducted to examine the persistence of disorder with increasing temperature for both formation methods. After ice formation, the ices were cooled to ~91 K, then heated at a rate of 1 K min^{-1} with infrared spectra collected every 1 K. The 3-μm (3300 cm^{-1}) feature from spectra collected during the linear temperature ramp from 113 to 185 K is shown in Fig. 5 for ices formed from LAI (left column) and VD (right column) at the deposition temperatures of 91 K (a) and (b), 113 K (c) and (d), and 165 K (e) and (f).

The method-dependent differences in ice structure at every temperature persist with heating. The onset of crystallization to cubic ice at ~150 K[6,15,31,38,39,58,70] from ices formed at 91 and 113 K [Figs. 5(a)–5(d)] is indicated by the redshift of ~30 cm^{-1} with warming. This shift in position is not accompanied by a change in shape. These low temperature ices do not change spectral shape or appear completely crystalline until ~170 K, where the spectra resemble that of CI (Fig. 3) due to the combination of crystallization and desorption of the amorphous component. Spectral change alone is insufficient to determine whether crystallization or desorption is the driver of the increasing crystallinity.

Heating-driven changes in the spectra are less visible in ices formed at 165 K [Figs. 5(e) and 5(f)]. Vapor deposition produces ice that stays crystalline until desorption, which begins at ~170 K. LAI@165 produces ice that changes only slightly during heating: the splitting between the two main components at 2.9 μm (3400 cm^{-1}) and 3.1 μm (3200 cm^{-1}) becomes less drastic as higher temperatures allow more water molecules to become tetrahedrally coordinated. The O–H stretch does not otherwise change in appearance until the ice becomes completely crystalline starting at ~180 K. Apparent differences in crystallization temperatures can be attributed to ice thickness and phase-sensitive thermal conductivity.

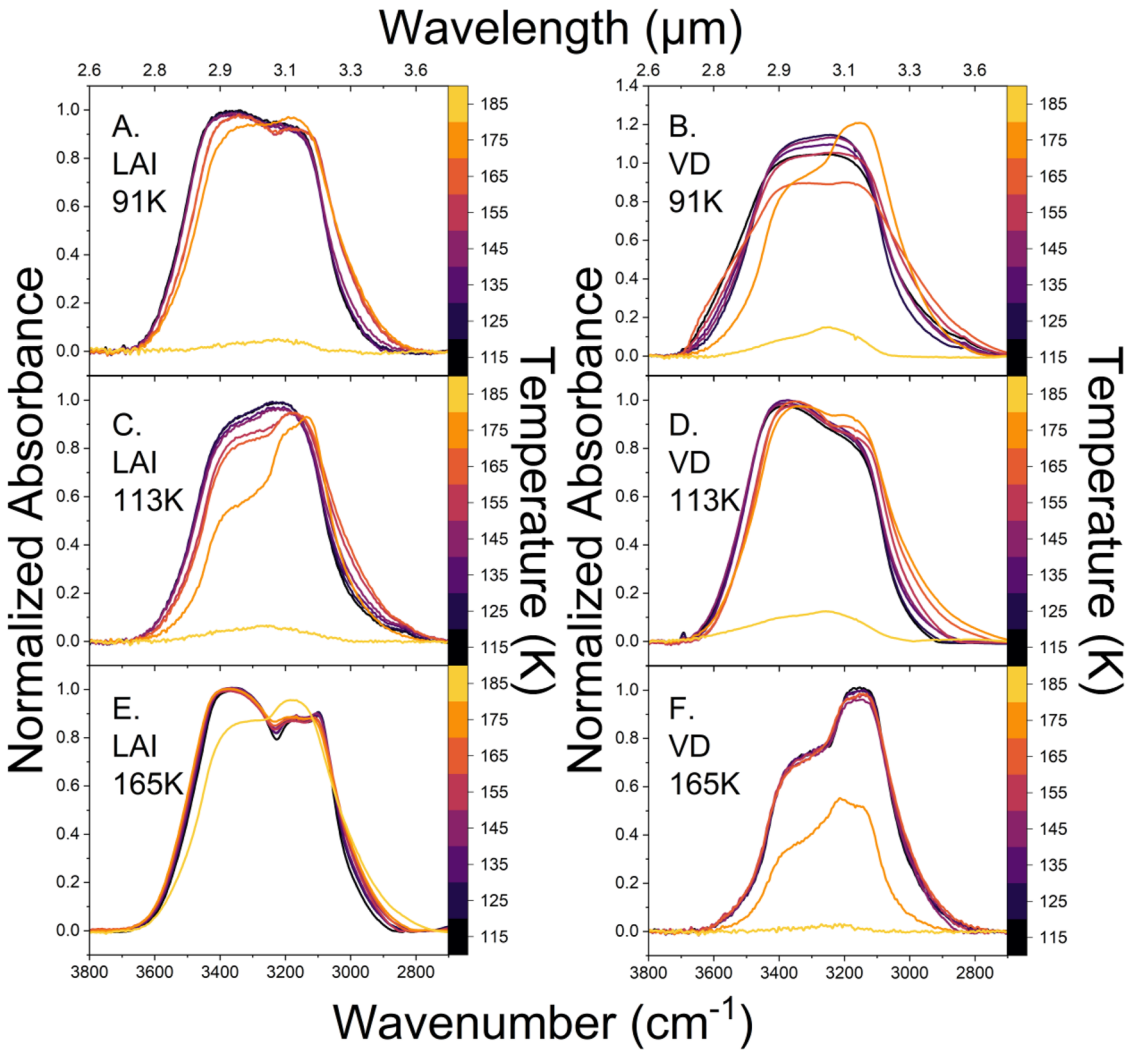

FIG. 5. Evolution of the 3-μm (3300 cm^{-1}) O–H stretch for ices formed by liquid aerosol injection (left column) and vapor deposition (right column). Ices were formed at the inset temperature [91 K (a) and (b), 113 K (c) and (d), 165 K (e) and (F)], then cooled to ~91 K. The spectra shown here were taken every 1 K during the heating process. At every temperature, the ices formed by the two methods appear different. Spectra are normalized to the intensity of the O–H stretch on formation.

Phase deconvolution

To determine the relative amounts of the well-defined CI, ASW, and HGW phases (Fig. 3), a Levenberg–Marquardt fitting procedure was used to constrain each normalized O–H stretch to a linear combination of the three phases shown in Fig. 3.[71,72] In this model, the shape and position of CI, ASW, and HGW were constrained, and only the amplitude could vary. The fitting results for ices formed at 91, 113, 135, and 140 K are shown in Fig. 6. This model was inspired by a fitting function that could distinguish between CI, ASW, and HGW, and was applied to both LAI and VD ices to determine if it could correctly assign HGW to only LAI ices.[17]

The χ^2 value of every fit produced by this three-phase fitting model is less than 2×10^{-3}. The spectra defined as phases for ASW (LAI@91) [Fig. 6(a)], HGW (LAI@113) [Fig. 6(c)], and CI (VD@165) (Fig. S5) are correctly identified with a χ^2 value of less than 5×10^{-4}. For the other ices, the total fit (dotted–dashed red line) accurately captures the peak position but varies in its ability to match the feature shape. The relative intensity of the two components of LAI@140 [Fig. 6(g)] does not match the model, as seen with the differences in the shape between the experimental data and the total fit and the larger χ^2 value than the other LAI ices shown, demonstrating that this ice cannot be classified as a unique combination of CI, ASW, and HGW.

Because the model is more sensitive to the peak position than to the shape of the 3-μm band, it is better at determining the presence or absence of crystalline ice than distinguishing between ASW and HGW. The peak position mainly reflects the relative amounts

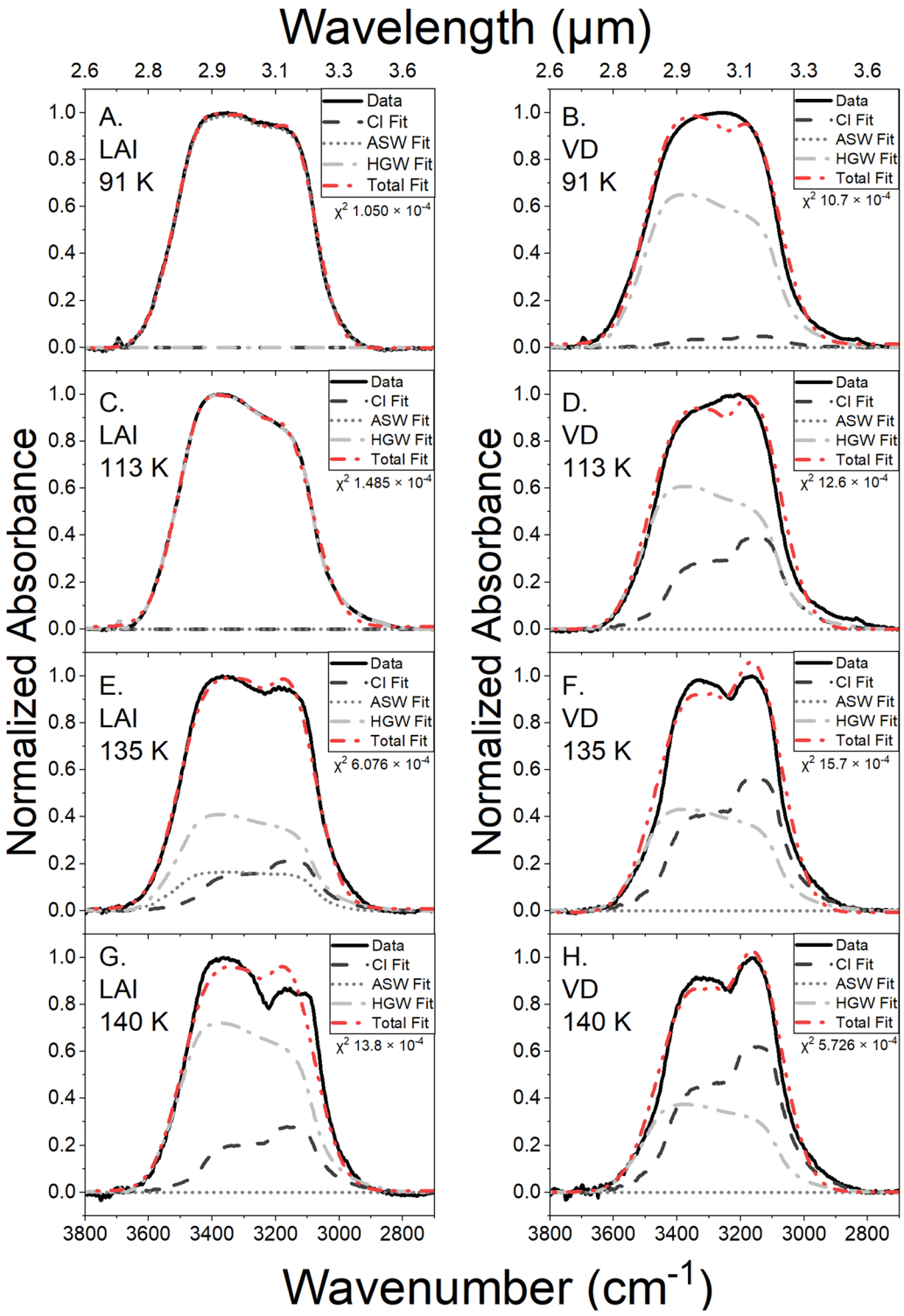

FIG. 6. Comparison between the normalized O–H stretch on ice formation (solid black) and three-phase model fitting for liquid aerosol injection (left column) and vapor deposition (right column). Ices were grown at 91 K (a) and (b), 113 K (c) and (d), 135 K (e) and (f), and 140 K (g) and (h). The contribution of each phase to the overall fit is shown scaled based on their relative amounts: crystalline ice (CI) in dashed dark gray, amorphous solid water (ASW) in dotted gray, and hyperquenched glassy water (HGW) in dotted–dashed light gray. The overall fit (sum of CI, ASW, and HGW fits) is shown in dotted–dashed red.

of tetrahedrally coordinated water molecules and dangling bonds,[27] so ASW and HGW have similar peak positions.[61] This similarity in position resulted in the model erroneously classifying all amorphous components of VD@113, for instance, as HGW. VD@113 should not contain any HGW due to the differences in freezing rates involved in vapor deposition and the formation of HGW. The three-phase fitting model applied to spectra collected during heating (Fig. S4) can track the increasing crystalline fraction of the ice but cannot consistently distinguish between ASW and HGW. Two-phase models (CI and HGW, CI and ASW, HGW and ASW) did not produce better fits for any ice based on the χ^2 values. A better model could be made with, narrower 3-μm phase definitions based on molecular beam deposition and a more constrained hyperquenching procedure, as it would allow the separation of HGW and ASW based on slightly different peak maxima as well as band shape.[17,61]

Data from the same experiments examining the temperature dependence of the H–O–H bend at 6 μm (1600 cm^{-1}) are shown in Fig. 7. At every temperature studied, the spectral shape appears different for ices formed through different methods, and the band depth at 6 μm (1600 cm^{-1}) is a factor of 2–3 greater for LAI than for VD. Due to the smaller band depth and signal-to-noise ratio, changes in position are less prominent and changes in intensity are harder to determine for the H–O–H bend than the O–H stretch. In general, heating causes a slight redshift in peak position above 155 K and a drastic reduction in feature intensity by 185 K. As stated previously, the feature has a significantly smaller oscillator strength relative to the O–H stretch; therefore, there is a smaller signal-to-noise ratio and a greater sensitivity to distortions induced by background subtraction. In addition, the H–O–H bend varies more with amplitude than with shape or position. Consequently, a model

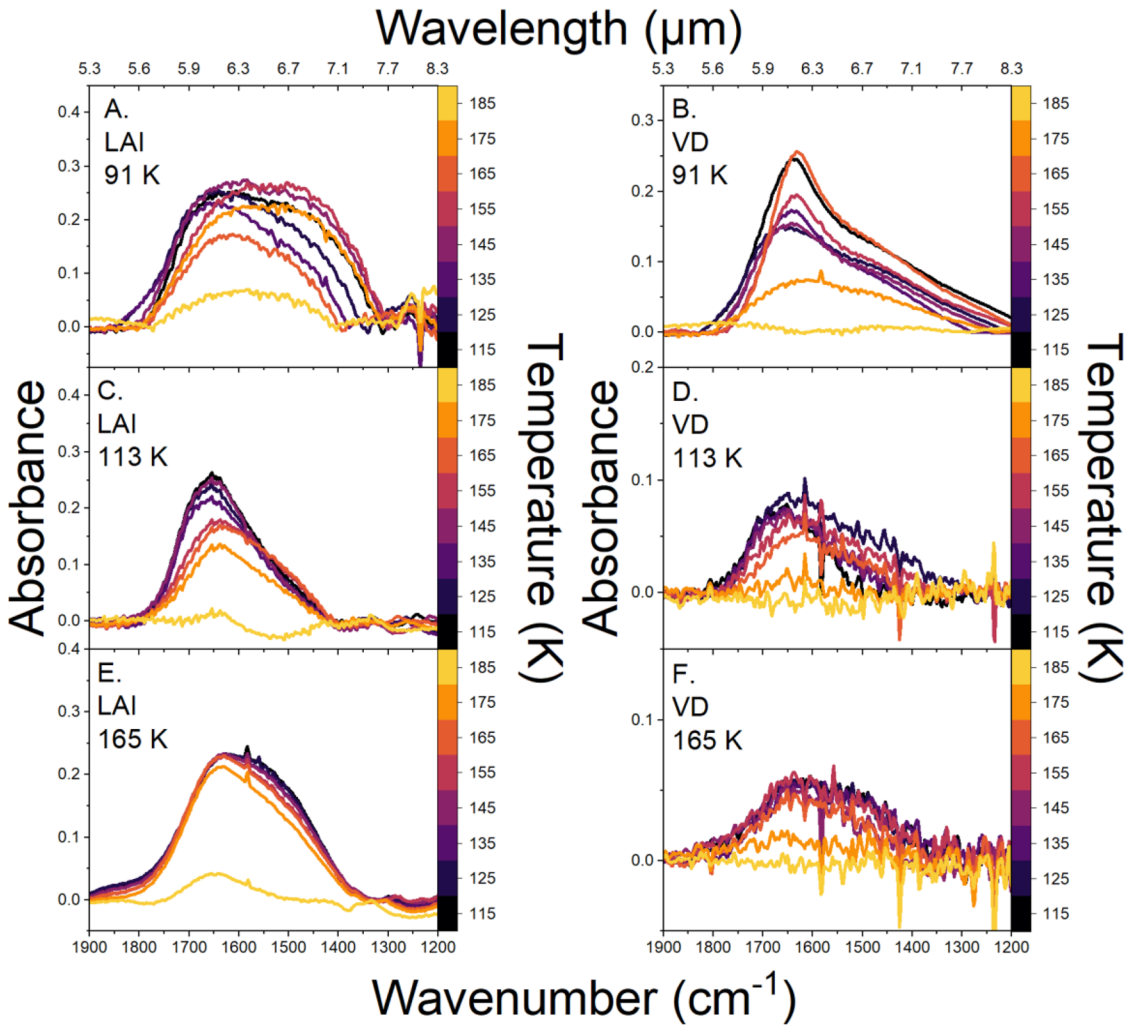

FIG. 7. Evolution of the 6-μm (1600 cm^{-1}) H–O–H bend for ices formed by liquid aerosol injection (left column) and vapor deposition (right column). Ices were formed at the inset temperature [91 K (a) and (b), 113 K (c) and (d), 165 K (e) and (f)], then cooled to ~91 K. The spectra shown here were taken at 10 K intervals during the heating process. The plots were normalized at the O–H stretch to preserve the intensity of the H–O–H bend relative to the O–H stretch.

for the 6-μm band similar to the described 3-μm band three-phase fit model did not produce meaningful results. Perfectly crystalline bulk ice would have no 6-μm band, since every water molecule would be completely tetrahedrally coordinated. Therefore, the presence of any 6-μm feature can be attributed to amorphous ice components and surface water molecules that are not fully tetrahedrally coordinated.[27] This bending feature is therefore useful in determining the presence of amorphous ice rather than in drawing conclusions about the amount of crystalline ice. Qualitatively, the H–O–H bend results support the conclusions from the O–H stretch: VD produces more ordered structures than LAI, and more ordered structures have a smaller 6-μm feature. LAI shows a broader feature than VD, which is attributed to IR-active hydrated protons.[68,69]

The data presented are consistent with the claim that ASW and HGW are different amorphous ice phases that vary in porosity and density.[4,11,17,19,30,73,74] HGW is less porous and denser, and the more tightly packed water molecules cause it to have fewer tetrahedrally coordinated molecules than ASW. Previous experiments have demonstrated that VD with a molecular beam at low temperatures (77 K) appears more like HGW, while the same method at warmer temperatures (115 K) produces amorphous solid water that appears more like the LDA spectrum used here for ASW.[17] Similar behavior for the onset temperature of the cubic phase transition is also expected for similarly disordered ices[37] since differences in porosity have no impact on the kinetics or mechanism of crystallization.[35] As predicted, ices in this study formed at a low temperature experience a crystallization regime starting at 150 K for both liquid aerosol injection and vapor deposition. However, until the ices begin to crystallize, their IR spectra remain different even with heating. A small difference in peak positions of 8 cm^{-1} for HGW and ASW has been documented for ices formed through molecular beam deposition,[17,61] but the ice thicknesses and less constrained VD and LAI processes in this study make that difference undetectable. The difference in spectral shapes, however, is still apparent, confirming that ASW and HGW are different phases.

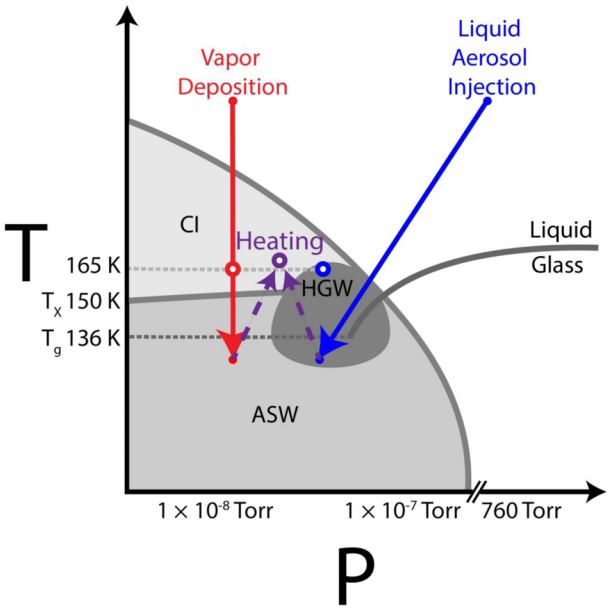

FIG. 8. Qualitative phase diagram of liquid aerosol injection and vapor deposition on formation and heating for ices formed at ~113 K. Liquid aerosol injection involves decreases in temperature and pressure fast enough to prevent crystallization, instead creating HGW. Amorphous solid water forms directly from the vapor phase in vapor deposition. Upon heating, both ices undergo a glass transition followed by crystallization. Open circles at 165 K represent ice formed at 165 K through both methods.

Figure 8 summarizes the temperature and pressure changes that ices experience during formation and heating. Injected water experiences a large drop in temperature and pressure to form HGW, and this supercooling process occurs fast enough that the water does not crystallize. Water that forms ASW through vapor deposition does not undergo pressure changes, and instead the molecules freeze individually via a statistical "hit-and-stick" process. HGW and ASW occupy neighboring places in the phase diagram. With heating under constant pressure, both phases undergo a glass transition at 136 K, then begin crystallization at 150 K. This diagram does not contain exact numerical fractions of crystalline components but can represent the differences in structure seen in Fig. 2, represented by open circles.

CONCLUSIONS

Ices formed through rapid freezing of a liquid aerosol have less ordered structures than ices formed through slow freezing from a vapor, including at temperatures warm enough to favor crystallinity. The phase-sensitive O–H stretch at 3 μm (3300 cm^{-1}) and H–O–H bend at 6 μm (1600 cm^{-1}) show these structural differences and how they evolve with heating. The shape of the 3-μm feature is most useful for determining the presence of crystalline ice, while the intensity of the 6-μm feature compared to the 3-μm band is most useful for determining the presence of amorphous ice. Comparison of these two spectral features represents a more comprehensive treatment of phase-sensitive infrared spectra. The observed behavior during heating of ices formed through different methods but at the same temperature is consistent with amorphous solid water ice, produced through vapor deposition, and hyperquenched glassy water, produced through liquid aerosol injection, being structurally different.

Ices grown under HV conditions are typically mixtures of coexisting phases, and the relative amount of each phase depends upon the deposition method and temperature. LAI produces HGW without going through any crystallization. There is clear liquid-like behavior at the glass transition during VD at 135 K and LAI at 165 K, which is manifested mainly by examining the 6-μm (1600 cm^{-1}) band of water. This band is rather important with respect to understanding hydrogen bond interactions and an important complementary diagnostic of hydrogen bonding in the liquid phase and disordered ice samples. Further research is needed to compare these formation methods with mixtures more complicated than pure water, especially for applications to astrophysical ices such as those formed through cryovolcanism or other flash-freezing processes.

SUPPLEMENTARY MATERIAL

Supplementary material figures include the change in voltage during a HeNe laser ice thickness measurement (see Experimental

Approach), a non-normalized version of Fig. 4, a zoomed-in version of Fig. 4 focusing on the dangling bonds at 2.70 μm (3700 cm^{-1}), the evolution of the fraction of ice corresponding to CI, ASW, and HGW (see Fig. 6 and accompanying text), and the phase fitting for VD@165.

ACKNOWLEDGMENTS

This work was directly supported by the NASA Solar System Exploration Research Virtual Institute (SSERVI) under Cooperative Agreement No. NNH22ZDA020C (CLEVER) and Grant No. 80NSSC23M0229.

AUTHOR DECLARATIONS

Conflict of Interest

The authors have no conflicts to disclose.

Author Contributions

Christina E. Buffo: Formal analysis (equal); Investigation (equal); Methodology (equal); Writing – original draft (equal); Writing – review & editing (equal). **Brant M. Jones**: Methodology (supporting); Supervision (supporting); Writing – review & editing (equal). **Thomas M. Orlando**: Conceptualization (equal); Funding acquisition (equal); Methodology (equal); Supervision (equal); Writing – review & editing (equal).

DATA AVAILABILITY

The data that support the findings of this study are openly available in the Georgia Tech Repository at https://hdl.handle.net/1853/77038.

REFERENCES

[1]T. Loerting, K. Winkel, M. Seidl, M. Bauer, C. Mitterdorfer, P. H. Handle, C. G. Salzmann, E. Mayer, J. L. Finney, and D. T. Bowron, "How many amorphous ices are there?," Phys. Chem. Chem. Phys. **13**(19), 8783–8794 (2011).
[2]J. Bachler, J. Giebelmann, and T. Loerting, "Experimental evidence for glass polymorphism in vitrified water droplets," Proc. Natl. Acad. Sci. U. S. A. **118**(30), e2108194118 (2021).
[3]A. Rosu-Finsen, M. B. Davies, A. Amon, H. Wu, A. Sella, A. Michaelides, and C. G. Salzmann, "Medium-density amorphous ice," Science **379**(6631), 474–478 (2023).
[4]A. Eltareb, G. E. Lopez, and N. Giovambattista, "A continuum of amorphous ices between low-density and high-density amorphous ice," Commun. Chem. **7**(1), 36 (2024).
[5]M. B. Davies, A. Rosu-Finsen, C. G. Salzmann, and A. Michaelides, "How crystalline is low-density amorphous ice?," arXiv:2305.03057 (2024).
[6]G. A. Kimmel, K. P. Stevenson, Z. Dohnálek, R. S. Smith, and B. D. Kay, "Control of amorphous solid water morphology using molecular beams. I. Experimental results," J. Chem. Phys. **114**(12), 5284–5294 (2001).
[7]R. S. Smith, T. Zubkov, Z. Dohnálek, and B. D. Kay, "The effect of the incident collision energy on the porosity of vapor-deposited amorphous solid water films," J. Phys. Chem. B **113**(13), 4000–4007 (2009).
[8]K. P. Stevenson, G. A. Kimmel, Z. Dohnálek, R. S. Smith, and B. D. Kay, "Controlling the morphology of amorphous solid water," Science **283**(5407), 1505–1507 (1999).
[9]E. Mayer and R. Pletzer, "Astrophysical implications of amorphous ice—A microporous solid," Nature **319**(6051), 298–301 (1986).
[10]T. Hama and N. Watanabe, "Surface processes on interstellar amorphous solid water: Adsorption, diffusion, tunneling reactions, and nuclear-spin conversion," Chem. Rev. **113**(12), 8783–8839 (2013).
[11]A. Hallbrucker, E. Mayer, and G. P. Johari, "The heat capacity and glass transition of hyperquenched glassy water," Philos. Mag. B **60**(2), 179–187 (1989).
[12]I. Kohl, L. Bachmann, A. Hallbrucker, E. Mayer, and T. Loerting, "Liquid-like relaxation in hyperquenched water at ≤140 K," Phys. Chem. Chem. Phys. **7**(17), 3210–3220 (2005).
[13]E. Mayer, "New method for vitrifying water and other liquids by rapid cooling of their aerosols," J. Appl. Phys. **58**(2), 663–667 (1985).
[14]T. Loerting, C. Salzmann, I. Kohl, E. Mayer, and A. Hallbrucker, "A second distinct structural 'state' of high-density amorphous ice at 77 K and 1 bar," Phys. Chem. Chem. Phys. **3**(24), 5355–5357 (2001).
[15]T. Reinot, N. C. Dang, and R. Jankowiak, "Hyperquenched glassy water and hyperquenched glassy ethanol probed by single molecule spectroscopy," J. Phys. Chem. B **113**(13), 4303–4313 (2009).
[16]Y. C. Wu, J. Jiang, S. J. Wang, A. Kallis, and P. G. Coleman, "Porosity and crystallization of water ice films studied by positron and positronium annihilation," Phys. Rev. B **84**(6), 064123 (2011).
[17]L. Kringle, W. A. Thornley, B. D. Kay, and G. A. Kimmel, "Reversible structural transformations in supercooled liquid water from 135 to 245 K," Science **369**(6510), 1490–1492 (2020).
[18]K. Winkel, D. T. Bowron, T. Loerting, E. Mayer, and J. L. Finney, "Relaxation effects in low density amorphous ice: Two distinct structural states observed by neutron diffraction," J. Chem. Phys. **130**(20), 204502 (2009).
[19]D. T. Bowron, J. L. Finney, A. Hallbrucker, I. Kohl, T. Loerting, E. Mayer, and A. K. Soper, "The local and intermediate range structures of the five amorphous ices at 80 K and ambient pressure: A Faber-Ziman and Bhatia-Thornton analysis," J. Chem. Phys. **125**(19), 194502 (2006).
[20]V. Fuentes-Landete, C. Mitterdorfer, P. Handle, G. Ruiz, J. Bernard, A. Bogdan, M. Seidl, K. Amann-Winkel, J. Stern, and S. Fuhrmann, "Crystalline and amorphous ices," in *Proceedings of the International School of Physics Enrico Fermi* (IOS Press, 2015), pp. 173–208.
[21]H. Li, A. Karina, M. Ladd-Parada, A. Späh, F. Perakis, C. Benmore, and K. Amann-Winkel, "Long-range structures of amorphous solid water," J. Phys. Chem. B **125**(48), 13320–13328 (2021).
[22]K. Amann-Winkel, R. Böhmer, F. Fujara, C. Gainaru, B. Geil, and T. Loerting, "Colloquium: Water's controversial glass transitions," Rev. Mod. Phys. **88**(1), 011002 (2016).
[23]W. Hagen and A. G. G. M. Tielens, "The librational region in the spectrum of amorphous solid water and ice I_c between 10 and 140 K," Spectrochim. Acta, Part A **38**(10), 1089–1094 (1982).
[24]J. E. Bertie and E. Whalley, "Infrared spectra of ices Ih and Ic in the range 4000 to 350 cm^{-1}," J. Chem. Phys. **40**(6), 1637–1645 (1964).
[25]A. Karina, T. Eklund, C. M. Tonauer, H. Li, T. Loerting, and K. Amann-Winkel, "Infrared spectroscopy on equilibrated high-density amorphous ice," J. Phys. Chem. Lett. **13**(34), 7965–7971 (2022).
[26]E. Whalley, "A detailed assignment of the O–H stretching bands of ice I," Can. J. Chem. **55**(19), 3429–3441 (1977).
[27]J. P. Devlin, J. Sadlej, and V. Buch, "Infrared spectra of large H_2O clusters: New understanding of the elusive bending mode of ice," J. Phys. Chem. A **105**(6), 974–983 (2001).
[28]C. I. Honniball, P. G. Lucey, S. Li, S. Shenoy, T. M. Orlando, C. A. Hibbitts, D. M. Hurley, and W. M. Farrell, "Molecular water detected on the sunlit Moon by SOFIA," Nat. Astron. **5**(2), 121–127 (2020).
[29]L. Starukhina, "Water detection on atmosphereless celestial bodies: Alternative explanations of the observations," J. Geophys. Res.: Planets **106**(E7), 14701–14710, https://doi.org/10.1029/2000je001307 (2001).
[30]A. Hallbrucker, E. Mayer, and G. P. Johari, "Glass-liquid transition and the enthalpy of devitrification of annealed vapor-deposited amorphous solid water: A comparison with hyperquenched glassy water," J. Phys. Chem. **93**(12), 4986–4990 (1989).

[31] M. T. Sieger and T. M. Orlando, "Effect of surface roughness on the electron-stimulated desorption of D^+ from microporous D_2O ice," Surf. Sci. **390**(1–3), 92–96 (1997).
[32] D. D. Klug, "Glassy water," Science **294**(5550), 2305–2306 (2001).
[33] U. Raut, M. Famá, B. D. Teolis, and R. A. Baragiola, "Characterization of porosity in vapor-deposited amorphous solid water from methane adsorption," J. Chem. Phys. **127**(20), 204713 (2007).
[34] A. Potapov, C. Jäger, and T. Henning, "Temperature programmed desorption of water ice from the surface of amorphous carbon and silicate grains as related to planet-forming disks," Astrophys. J. **865**(1), 58 (2018).
[35] K. Harada, T. Sugimoto, F. Kato, K. Watanabe, and Y. Matsumoto, "Thickness dependent homogeneous crystallization of ultrathin amorphous solid water films," Phys. Chem. Chem. Phys. **22**(4), 1963–1973 (2020).
[36] Y. Oba, N. Miyauchi, H. Hidaka, T. Chigai, N. Watanabe, and A. Kouchi, "Formation of compact amorphous H_2O ice by codeposition of hydrogen atoms with oxygen molecules on grain surfaces," Astrophys. J. **701**(1), 464 (2009).
[37] B. Maté, Y. Rodríguez-Lazcano, and V. J. Herrero, "Morphology and crystallization kinetics of compact (HGW) and porous (ASW) amorphous water ice," Phys. Chem. Chem. Phys. **14**(30), 10595–10602 (2012).
[38] P. Jenniskens, S. F. Banham, D. F. Blake, and M. R. S. McCoustra, "Liquid water in the domain of cubic crystalline ice I_c," J. Chem. Phys. **107**(4), 1232–1241 (1997).
[39] G. P. Johari, "Liquid state of low-density pressure-amorphized ice above its T_g," J. Phys. Chem. B **102**(24), 4711–4714 (1998).
[40] P. B. Gooderum and D. M. Bushnell, "Measurement of mean drop sizes for sprays from superheated waterjets," J. Spacecr. Rockets **6**(2), 197–198 (1969).
[41] R. E. Steddum, "Characteristics of water sprays under vacuum conditions," Ph.D. dissertation (Louisiana State University and Agricultural and Mechanical College, 1971).
[42] R. D. Reitz, "A photographic study of flash-boiling atomization," Aerosol Sci. Technol. **12**(3), 561–569 (1990).
[43] R. T. Garrod, "Simulations of ice chemistry in cometary nuclei," Astrophys. J. **884**(1), 69 (2019).
[44] W. A. Brown, S. Viti, A. J. Wolff, and A. S. Bolina, "Laboratory investigations of the role of the grain surface in astrochemical models," Faraday Discuss. **133**, 113–124 (2006).
[45] L. Hornekær, A. Baurichter, V. V. Petrunin, A. C. Luntz, B. D. Kay, and A. Al-Halabi, "Influence of surface morphology on D_2 desorption kinetics from amorphous solid water," J. Chem. Phys. **122**(12), 124701 (2005).
[46] C. M. Tonauer, L.-R. Fidler, J. Giebelmann, K. Yamashita, and T. Loerting, "Nucleation and growth of crystalline ices from amorphous ices," J. Chem. Phys. **158**(14), 141001 (2023).
[47] H. S. Cao, "Formation and crystallization of low-density amorphous ice," J. Phys. D: Appl. Phys. **54**(20), 203002 (2021).
[48] R. Scott Smith, C. Huang, E. K. L. Wong, and B. D. Kay, "Desorption and crystallization kinetics in nanoscale thin films of amorphous water ice," Surf. Sci. **367**(1), L13–L18 (1996).
[49] V. Buch and J. P. Devlin, "A new interpretation of the OH-stretch spectrum of ice," J. Chem. Phys. **110**(7), 3437–3443 (1999).
[50] R. L. Hudson, M. H. Moore, and P. A. Gerakines, "The Formation of cyanate ion (OCN^-) in interstellar ice analogs," Astrophys. J. **550**(2), 1140 (2001).
[51] H. M. Cuppen, C. Walsh, T. Lamberts, D. Semenov, R. T. Garrod, E. M. Penteado, and S. Ioppolo, "Grain surface models and data for astrochemistry," Space Sci. Rev. **212**(1–2), 1–58 (2017).
[52] I. Langmuir, "The adsorption of gases on plane surfaces of glass, mica and platinum," J. Am. Chem. Soc. **40**(9), 1361–1403 (1918).
[53] B. G. Koehler, A. M. Middlebrook, and M. A. Tolbert, "Characterization of model polar stratospheric cloud films using Fourier transform infrared spectroscopy and temperature programmed desorption," J. Geophys. Res.: Atmos. **97**(D8), 8065–8074, https://doi.org/10.1029/91jd01844 (1992).
[54] J.-B. Bossa, K. Isokoski, D. M. Paardekooper, M. Bonnin, E. P. van der Linden, T. Triemstra, S. Cazaux, A. G. G. M. Tielens, and H. Linnartz, "Porosity measurements of interstellar ice mixtures using optical laser interference and extended effective medium approximations," Astron. Astrophys. **561**, A136 (2014).
[55] D. R. Haynes, N. J. Tro, and S. M. George, "Condensation and evaporation of water on ice surfaces," J. Phys. Chem. **96**(21), 8502–8509 (1992).
[56] B. Maté, A. Medialdea, M. A. Moreno, R. Escribano, and V. J. Herrero, "Experimental studies of amorphous and polycrystalline ice films using FT-RAIRS," J. Phys. Chem. B **107**(40), 11098–11108 (2003).
[57] W. Hagen, A. G. G. M. Tielens, and J. M. Greenberg, "The infrared spectra of amorphous solid water and ice I_c between 10 and 140 K," Chem. Phys. **56**(3), 367–379 (1981).
[58] F. Bensebaa and T. H. Ellis, "Water at surfaces: What can we learn from vibrational spectroscopy?," Prog. Surf. Sci. **50**(1), 173–185 (1995).
[59] R. S. Smith, Z. Dohnálek, G. A. Kimmel, G. Teeter, P. Ayotte, J. L. Daschbach, and B. D. Kay, "Molecular beam studies of nanoscale films of amorphous solid water," in *Water in Confining Geometries* (Springer, 2003), pp. 337–357.
[60] E. H. G. Backus, M. L. Grecea, A. W. Kleyn, and M. Bonn, "Surface crystallization of amorphous solid water," Phys. Rev. Lett. **92**(23), 236101 (2004).
[61] L. Kringle, B. D. Kay, and G. A. Kimmel, "Structural relaxation of water during rapid cooling from ambient temperatures," J. Chem. Phys. **159**(6), 064509 (2023).
[62] J. P. Devlin, "Structure, spectra, and mobility of low-pressure ices: Ice I, amorphous solid water, and clathrate hydrates at T < 150 K," J. Geophys. Res.: Planets **106**(E12), 33333–33349, https://doi.org/10.1029/2000je001301 (2001).
[63] S. Kaya, J. Weissenrieder, D. Stacchiola, S. Shaikhutdinov, and H.-J. Freund, "Formation of an ordered ice layer on a thin silica film," J. Phys. Chem. C **111**(2), 759–764 (2007).
[64] R. M. Mastrapa, S. A. Sandford, T. L. Roush, D. P. Cruikshank, and C. M. Dalle Ore, "Optical constants of amorphous and crystalline H_2O-ice: 2.5–22 μm (4000–455 cm^{-1}) optical constants of H_2O-ice," Astrophys. J. **701**(2), 1347 (2009).
[65] R. Lecourt, P. Barricau, and J. Steelant, "Spray velocity and drop size measurements in flashing conditions," Atomization Sprays **19**(2), 103–133 (2009).
[66] C. Medcraft, D. McNaughton, C. D. Thompson, D. R. T. Appadoo, S. Bauerecker, and E. G. Robertson, "Water ice nanoparticles: Size and temperature effects on the mid-infrared spectrum," Phys. Chem. Chem. Phys. **15**(10), 3630–3639 (2013).
[67] Y. Xu, N. G. Petrik, R. S. Smith, B. D. Kay, and G. A. Kimmel, "Growth rate of crystalline ice and the diffusivity of supercooled water from 126 to 262 K," Proc. Natl. Acad. Sci. U. S. A. **113**(52), 14921–14925 (2016).
[68] A. M. Duffin and R. J. Saykally, "Electrokinetic power generation from liquid water microjets," J. Phys. Chem. C **112**(43), 17018–17022 (2008).
[69] J. Xu, Y. Zhang, and G. A. Voth, "Infrared spectrum of the hydrated proton in water," J. Phys. Chem. Lett. **2**(2), 81–86 (2011).
[70] A. S. Bolina, A. J. Wolff, and W. A. Brown, "Reflection absorption infrared spectroscopy and temperature-programmed desorption studies of the adsorption and desorption of amorphous and crystalline water on a graphite surface," J. Phys. Chem. B **109**(35), 16836–16845 (2005).
[71] K. Levenberg, "A method for the solution of certain non-linear problems in least squares," Q. Appl. Math. **2**(2), 164–168 (1944).
[72] D. W. Marquardt, "An algorithm for least-squares estimation of nonlinear parameters," J. Soc. Ind. Appl. Math. **11**(2), 431–441 (1963).
[73] T. E. Gartner, "Linking amorphous ice and supercooled liquid water," Proc. Natl. Acad. Sci. U. S. A. **118**(34), e2112191118 (2021).
[74] P. G. Debenedetti and H. E. Stanley, "Supercooled and glassy water," Phys. Today **56**(6), 40–46 (2003).